Received: 28 July 2022 | Revised: 11 November 2022 | Accepted: 13 December 2022

DOI: 10.1002/ijc.34447

TUMOR IMMUNOLOGY AND MICROENVIRONMENT

IJC INTERNATIONAL JOURNAL of CANCER

Extracellular vesicles secreted by triple-negative breast cancer stem cells trigger premetastatic niche remodeling and metastatic growth in the lungs

Patricia González-Callejo[1,2] | Petra Gener[1,2] | Zamira V. Díaz-Riascos[1,2,3] | Sefora Conti[4] | Patricia Cámara-Sánchez[1,2,3] | Roger Riera[5,6] | Sandra Mancilla[1,2,3] | Miguel García-Gabilondo[7] | Vicente Peg[8,9] | Diego Arango[10,11] | Anna Rosell[7] | Anna Labernadie[4] | Xavier Trepat[2,4,12] | Lorenzo Albertazzi[5,6] | Simó Schwartz Jr[1,2] | Joaquin Seras-Franzoso[1,2,13] | Ibane Abasolo[1,2,3]

[1]Drug Delivery & Targeting, Vall d'Hebron Institut de Recerca (VHIR), Universitat Autònoma de Barcelona (UAB), Barcelona, Spain

[2]Networking Research Center on Bioengineering, Biomaterials and Nanomedicine (CIBER-BBN), Instituto de Salud Carlos III, Madrid, Spain

[3]Functional Validation & Preclinical Research (FVPR), Vall d·Hebron Institut de Recerca (VHIR), Universitat Autònoma de Barcelona (UAB), Passeig de la Vall d'Hebron, Barcelona, Spain

[4]Integrative Cell and Tissue Dynamics Group, Institute for Bioengineering of Catalonia (IBEC), Barcelona, Spain

[5]Nanoscopy for Nanomedicine Group, Institute for Bioengineering of Catalonia (IBEC), Barcelona, Spain

[6]Department of Biomedical Engineering, Institute for Complex Molecular Systems (ICMS), Eindhoven University of Technology, Eindhoven, Netherlands

[7]Neurovascular Research Laboratory, Vall d·Hebron Institut de Recerca (VHIR), Universitat Autònoma de Barcelona (UAB), Passeig Vall d'Hebron, Barcelona, Spain

[8]Department of Pathology, Vall d'Hebron University Hospital, Universitat Autònoma de Barcelona (UAB), Barcelona, Spain

[9]Spanish Biomedical Research Network Centre in Oncology (CIBERONC), Instituto de Salud Carlos III, Madrid, Spain

[10]Department of Molecular Oncology, Biomedical Research Institute of Lleida, Lleida, Spain

[11]Biomedical Research in Digestive Tract Tumors, Vall d'Hebron Research Institute (VHIR), Universitat Autònoma de Barcelona (UAB), Passeig de la Vall d'Hebron, Barcelona, Spain

[12]Catalan Institution for Research and Advanced Studies (ICREA), Passeig Lluís Companys, Barcelona, Spain

[13]Department of Genetics and Microbiology, Universitat Autònoma de Barcelona (UAB), Bellaterra, Spain

Correspondence
Simó Schwartz Jr, Networking Research Center on Bioengineering, Biomaterials and Nanomedicine (CIBER-BBN), Instituto de Salud Carlos III, 28029 Madrid, Spain.
Email: simo.schwartz@vhir.org

Joaquin Seras-Franzoso, Drug Delivery & Targeting, Vall d'Hebron Institut de Recerca (VHIR), Universitat Autònoma de Barcelona (UAB), Passeig Vall d'Hebron, 119-129, 08035

Abstract

Tumor secreted extracellular vesicles (EVs) are potent intercellular signaling platforms. They are responsible for the accommodation of the premetastatic niche (PMN) to support cancer cell engraftment and metastatic growth. However, complex cancer cell composition within the tumor increases also the heterogeneity among cancer secreted EVs subsets, a functional diversity that has been poorly explored. This phenomenon is particularly relevant in highly plastic and heterogenous triple-negative breast cancer

Abbreviations: ALDH1A1, aldehyde dehydrogenase 1; α-SMA, alpha smooth actin; BCA, bicinchoninic acid assay; BLI, bioluminescence imaging; b.v, blood vessels; CAFs, cancer-associated fibroblast; CM, conditioned medium; CSC, cancer stem cell; DCC, differentiated cancer cell; ECM, extracellular matrix; ERα, estrogen receptor alpha; EV, extracellular vesicle; FACS, fluorescence-activated cell sorting; FLI, fluorescence imaging; HER2, epidermal growth factor 2 receptor; iCAFs, inflammatory CAFs; IDC, invasive ductal breast carcinoma; ITG, integrin; i.v., intravenously; MET, metastasis; myCAFs, myofibroblastic CAFs; PMN, premetastatic niche; PR, progesterone receptor; PTX, paclitaxel; SN, supernatant; TME, tumor microenvironment; TNBC, triple-negative breast cancer.

Barcelona, Spain.
Email: joaquin.seras@vhir.org

Funding information
Agència de Gestió d·Ajuts Universitaris i de Recerca, Grant/Award Numbers: 2017-SGR-1427, 2017-SGR-638; Centro de Investigación Biomédica en Red en Bioingeniería, Biomateriales y Nanomedicina, Grant/Award Number: PENTRI-2; Fundación Bancaria Caixa d'Estalvis i Pensions de Barcelona, Grant/Award Number: LCF/BQ/PR18/11640001; Fundación Científica Asociación Española Contra el Cáncer, Grant/Award Number: AIO14142112SERA; Instituto de Salud Carlos III, Grant/Award Numbers: ISCIII PI20/01474, ISCIIIPI22/01301

(TNBC), in which a significant representation of malignant cancer stem cells (CSCs) is displayed. Herein, we selectively isolated and characterized EVs from CSC or differentiated cancer cells (DCC; EVs^{CSC} and EVs^{DCC}, respectively) from the MDA-MB-231 TNBC cell line. Our results showed that EVs^{CSC} and EVs^{DCC} contain distinct bioactive cargos and therefore elicit a differential effect on stromal cells in the TME. Specifically, EVs^{DCC} activated secretory cancer associated fibroblasts (CAFs), triggering IL-6/IL-8 signaling and sustaining CSC phenotype maintenance. Complementarily, EVs^{CSC} promoted the activation of α-SMA+ myofibroblastic CAFs subpopulations and increased the endothelial remodeling, enhancing the invasive potential of TNBC cells in vitro and in vivo. In addition, solely the EVs^{CSC} mediated signaling prompted the transformation of healthy lungs into receptive niches able to support metastatic growth of breast cancer cells.

KEYWORDS
cancer cell plasticity, extracellular vesicles, premetastatic niche, triple-negative breast cancer, tumor microenvironment

What's new?

Cancer-secreted extracellular vesicles (EVs) are involved in premetastatic niche (PMN) conditioning, which promotes disease spread. However, diversity among cancer-secreted EVs, which is related to heterogeneity in tumor cells, often is disregarded in the context of cancer progression. Here, the authors examined the activity of cancer cell-secreted EVs in triple-negative breast cancer (TNBC) at distinct states of tumor cell differentiation. Experiments show that EVs differ radically in their activities, depending on their original cancer cell subtype. Specifically, signaling systems involving EVs secreted by cancer stem cells were found to drive PMN remodeling in TNBC models, both in vitro and in vivo.

1 | INTRODUCTION

Triple-negative breast cancer (TNBC) is a group of particularly aggressive breast cancer subtypes representing nearly 15% of all breast tumors.[1,2] At the molecular level, TNBC is characterized by the lack of expression of therapeutic targets such as estrogen receptor alpha (ERα), progesterone receptor (PR) and epidermal growth factor 2 receptor (HER2). Besides, TNBC tumors are markedly heterogeneous and cancer cells within them present significant levels of cell polyclonality and coexist in distinct phenotypic states, both phenomena related to cancer malignancy and drug resistance.[3,4]

Particularly, cancer stem cells (CSCs) are often over-represented in TNBCs and have been associated with the higher chemotherapy resistance, metastatic spread and tumor recurrence rates observed in TNBC patients.[5-7] CSC represent a fraction of nonspecialized cancer cells that exhibit stem cell-like features like self-renewal and differentiation potential. In addition, CSCs possess tumor-initiating capacity and are highly resistant to conventional chemotherapy. Such resistance is the result of combining an active molecular machinery, for example, high expression of drug efflux transporters like P-glycoprotein or detoxifying enzymes like aldehyde dehydrogenase 1 (ALDH1A1), with the capability to undergo quiescent states during adverse conditions or even enter dormancy for prolonged periods.[8,9]

Although CSCs origin and homeostasis within the tumor is not yet fully understood it is clear that TNBC cells are much more plastic entities than initially anticipated. In this sense, TNBC cells have been proved able to undergo phenotypic bidirectional transitions in vitro and in vivo, pulsing between CSC and differentiated cancer cell (DCC) states.[10-12] Moreover, there is evidence of multiple stimuli produced by the tumor microenvironment (TME) cell milieu involved in CSC regulation,[13-16] a phenomenon that is inextricably related to the gain of invasive potential, cancer spread, resistance to treatment and disease relapse. This intricate intercellular communication network is crucial for cancer progression and comprise small molecules like growth factors, hormones, metabolites and cytokines but also supramolecular entities such as extracellular vesicles (EVs).[17,18]

Remarkably, EVs reunite the appropriate features to act as central signal delivery platforms for intercellular communication. Secreted by virtually all cell types, EVs can load and deliver a broad range of bioactive molecules like proteins, lipids and nucleic acids.[19] Furthermore, EVs are stable in biological fluids and can reach distal sites within the body while providing stability and protection to their biological cargo.[20] Such versatility enables the exchange of complex and diverse messages between neighboring or distal cells. Specifically, in the cancer context, EVs have been shown to induce the transition of stromal cells such as mesenchymal stem cells,[21] fibroblasts,[22] endothelial cells[23] and immune cells[24,25] towards phenotypes more prone to foster tumoral growth, in primary tumors, but also in distant organs, facilitating the conditioning of the premetastatic niches (PMN).

Particularly interesting is the role of cancer cell derived EVs in fibroblast regulation. EVs from cancer cells have been shown to

upregulate NF-κβ signaling pathway driving fibroblasts activation towards Cancer Associated Fibroblasts (CAFs).[22] Upon activation, CAFs support tumor progression and metastasis by promoting local invasion, stimulating CSC occurrence or mediating in immune suppressive signaling.[26,27] The high heterogeneity of CAFs coupled to the lack of specific markers to unequivocally identify CAFs subsets has obstacled the unraveling of their distinct roles in cancer malignancy. However, two major general CAFs subtypes have been clustered based on their molecular signature combined with their ultimate function. On one hand, a myofibroblastic CAFs subset known as myCAFs, characterized by higher expression of alpha smooth actin (α-SMA) and significant production of extracellular matrix (ECM) proteins.[28] MyCAFs are known to exert a direct effect on local cancer invasion due their capacity to remodel the ECM.[29] On the other hand, a secretory subtype, named inflammatory CAFs (iCAFs) has been also identified. iCAFs are mainly defined by their abnormal over secretion of inflammatory cytokines and intervene as mediators of TME signaling, leading to immunosuppression events and fostering of CSC phenotypes.[14,30,31] Altogether, during cancer metastatic advance, the role of cancer cell derived EVs in CAFs, culminates in the generation of a receptive PMN, capable of attracting circulating cancer cells and supporting their growth far from their site of origin.

It is worth noting that, even though EVs' composition is largely determined by the cell source[32] and CSCs have been proposed as important mediators of TNBC malignancy, the study of EVs' contribution to cancer progression has generally disregarded the phenotypic state of the EVs-secreting cancer cells.

Here, we aimed to evaluate the role of EVs isolated from cancer cells at distinct differentiation states (CSC vs DCC) in TNBC, specifically in the context of metastatic disease and PMN conditioning.

2 | MATERIALS AND METHODS

2.1 | Cell lines and culture conditions

2.1.1 | Parental cell lines

Human breast MDA-MB-231 (RRID:CVCL_0062) cell line, human lung CCD-19Lu (RRID:CVCL_2382) were obtained from American Type Culture Collection (ATCC HTB-26, CCL-210, respectively). hCMEC/D3 cells (RRID:CVCL_U985) were gifted from Pierre-Olivier Couraud, CNRS, France. Patient derived Cancer Associated Fibroblasts from Invasive Ductal Breast Carcinoma (CAFs IDC) were gifted from Erik Sahai, Francis Crick Institute, UK.

2.1.2 | Genetically modified cell lines

MDA-MB-231.Fluc2-C19 and MDA-MB-231 ALDH:tdTomato cell lines were previously generated by our group.[12,33] MDA-MB-231 ALDH:tdTomato was employed for EVs^{CSC} and EVs^{DCC} production along the study.

Cell media composition is detailed in Data S1, Supporting Methods section. All cell cultures were propagated at 37°C and 5% CO_2 in a humidified incubator.

All human cell lines have been authenticated using STR profiling.

All the experiments were performed with mycoplasma-free cells.

2.2 | CSC isolation

CSC subpopulations from MDA-MB-231 ALDH:tdTomato were isolated according to their tdTomato expression in a FACS Aria cell sorter (BD Biosciences, Franklin Lakes, NJ). Representative scheme of cells sorting procedure is detailed in Figure S2C.

2.3 | Purification of EVs^{CSC} and EVs^{DCC}

Supernatants (SN) from MDA-MB-231 CSC and DCC cell cultures, after 48 hours incubation in EV-depleted medium, were centrifuged at increasing speeds: 300*g* at 4°C for 10 minutes, 2000*g*, 10 minutes 4°C and 10 000*g* 20 minutes 4°C to eliminate potential cellular and subcellular debris. Clarified SNs were concentrated through centrifugation at 5000*g*, 15 minutes, 4°C, using 300 000 kDa VIVAspin devices (Sartorius, Gottingen, Germany). EVs were then precipitated from concentrated SN by the addition of "Total Exosome Isolation Reagent" (Invitrogen, Waltham, MA) according to manufacturer's instructions and EVs resuspended in PBS.

2.4 | EVs characterization

CryoTEM morphometric assessment and particle size distribution and concentration were further studied by Nanoparticle Tracking Analysis (NTA) performed as described by Seras-Franzoso and co-workers.[34]

2.5 | RNA extraction and quantitative real time-qPCR

Total RNA was extracted from 300 000 cells using the RNeasy Micro Kit (Qiagen, Hilden, Germany) and the RNA obtained was reverse transcribed using a high Capacity cDNA Reverse Transcription Kit (Thermo Fisher Scientific, Waltham, MA) according to the manufacturer's instructions. The cDNA was amplified with specific primers (Table S1) by qPCR using a SYBR Green method (Thermo Fisher Scientific) in a 7500 Real time PCR system (Applied Biosystems, Waltham, MA). Relative normalized quantities (NRQ) were calculated using the comparative Ct method ($2^{-\Delta\Delta Ct}$) through Qbase software with two reference genes (hGAPDH and hActin) as endogenous controls. Further detail is available at Data S1, Supporting Methods section.

2.6 | Protein extraction and Western blotting

Cell pellets and EVs were lysed in Cell Lytic M reagent (Sigma-Aldrich, St. Louis, MO) and protein quantified using the bicinchoninic acid assay (BCA; Pierce Biotechnology, Waltham, MA). Twenty micrograms of of whole-cell lysates were separated by SDS-PAGE and transferred onto PVDF membranes (Merck Millipore, Burlington, MA). Membranes were blocked in 5% nonfat dry milk (w/v) in TBS buffer, 1 hour at RT. Targeted proteins were probed using primary antibodies (Table S2), O.N. at 4°C. Horseradish peroxidase (HRP)-conjugated secondary antibodies, anti-mouse (P0447, Dako) or anti-rabbit (P0217, Dako), were then added and incubated for 1 hour at room temperature. Membranes were developed using Immobilion HRP substrate (Merck Millipore) in a LI-COR Odyssey Fc imaging system. Band intensity on the blots was quantified using the ImageJ NIH software.

2.7 | 3D invasion assay

CAFs IDC and CCD-19Lu cells (200 000 cells) were seeded in a P10 plate. Then, cells were trypsinized to single-cell suspension, centrifuged and resuspended with 3 mL of culture medium containing 2 µL of CellTracker staining solution. After 30 minutes of incubation, cells were washed, counted and resuspended to reach a final concentration of 75×10^5 cells/mL. Hence, a cell suspension containing the two cell types at a 1:1 ratio and 0.25% methylcellulose solution in DMEM was prepared and 3D invasion assay was performed as described by Labernadie et al.[35,36]

2.8 | Cytokine and stem protein arrays

Cytokine antibody-pair-based assays (R&D Systems, ARY005B) were performed according to the manufacturer's protocol. In brief, 100 000 CCD-19Lu fibroblasts seeded in 6-well plates were cultured alone or treated with either EVs^{CSC} or EVs^{DCC}, 25 µg/mL per day during 3 days. Culture supernatants were next collected (CM) and added to the array membranes, O.N. at 4°C. Membranes were washed, incubated with a streptavidin-HRP-coupled antibody (1:2000) for 30 minutes at RT and developed using Chemi-Reagent Mix. Images were captured and visualized using the LI-COR Odyssey Fc imaging system and dot intensity was measured using ImageJ NIH software.

Human pluripotent stem cell antibody array (R&D Systems, ARY010) was performed in accordance with the manufacturer's instructions. Briefly, approximately 500 µg of total-EVs^{CSC} and EVs^{DCC} lysates were incubated with array membranes O.N. at 4°C. Membranes were then processed as described above.

2.9 | Tube formation assay

Capacity to promote vessel-like tube formation was assessed as described elsewhere.[37] hCMEC/D3 cells were treated with either 25 µg/mL EVS^{CSC} or EVS^{DCC} suspensions or basal media (as control condition). After O.N. incubation at 37°C and 5% CO_2 images were taken at four times and analyzed blindly using Wimtube online tool. Tube length, branching points and total loops were quantified. Control condition (basal media) was used as a reference value.

2.10 | In vivo experimentation

Female NOD.CB17-Prkdcscid/J mice (Charles River, MA) were kept in pathogen-free conditions and used at 6 weeks of age.

2.11 | EV fluorescent labeling

DiOC/DiD or DiR (Invitrogen) were supplemented to EVs^{CSC} and EVs^{DCC} to a concentration of 250 and 500 µg/mL, respectively, for 30 minutes at 37°C. Samples were then dialyzed (Slide-A-Lyzer MINI Dialysis Device, 3.5K MWCO, 0.1 mL, Thermo Scientific, Waltham, MA) against PBS, O.N. at 4°C.

2.12 | Biodistribution assay

EVs^{CSC} and EVs^{DCC} biodistribution studies were performed by intravenous administration of 300 µg DiR-labeled EVs^{CSC} or EVs^{DCC} through the tail vein of NOD/SCID mice. After 24 hours, animals were euthanized and ex vivo DiR-EVs localization was assessed using in an IVIS Spectrum equipment for image acquisition and Living Image Software to further quantify the fluorescent imaging (FLI). FLI signal was normalized to the weight of the wet tissue and represented as the percentage of total FLI per animal.

2.13 | Lung metastasis mice models

Three doses of 75 µg of EVs^{CSC} or EVs^{DCC}, corresponding $3.3 \pm 0.26 \times 10^8$ and $6.3 \pm 0.81 \times 10^8$ particles/bolus, respectively, were intravenously injected into female nude mice through the tail vein every other day. On the fifth day, 1×10^6 firefly luciferase-expressing MDA-MB-231.Fluc2-C19 cells were intravenously injected through the tail vein. After 2 months, lung metastasis were quantified by ex vivo bioluminescent imaging using IVIS Spectrum (PerkinElmer) and lung tissues were recovered for manual macrometastasis and micrometastasis counting and further processed for hematoxylin-eosin staining analysis and evaluation by a trained histopathologist.

2.14 | Immunohistochemistry

α-SMA was assessed in paraffin-embedded formalin fixed sections prepared as detailed in Data S1, Supporting Methods section.

α-SMA + CAFs infiltration and blood vessel occurrence in lung metastatic lesions were evaluated in 18 random sections per mice group. Covered areas by α-SMA + fibroblasts like cells was qualitatively scored and represented, staining score values ranging from 0 (0% positive area) to 3 (100% positive area). Each evaluation was made blindly by three independent observers. The number of blood vessels was quantitatively assessed by manually counting the number of α-SMA positive blood vessels. Subsequent mean score for both parameters was then calculated for each group.

2.15 | Statistical analysis

Bar graphs display mean value ± SE of the mean (SEM). Statistical analysis consisted in normality data distribution assessment by Kolmogorov-Smirnov test. Data fitting into a normal distribution, was submitted to unpaired Student's *t*-test, for single comparison of means, or one-way ANOVA for multiple comparisons. Otherwise, nonparametric Mann-Whitney test or Tukey test were employed for single and multiple mean comparisons, respectively.

Data represented as fold change (FC) were normalized following the X = Log (FC) function. Columns statistics were then used to assess the mean difference in comparison to a theoretical Log (FC) value equal to 0. The significance threshold was established at $P < .05$, and significance levels were schematically assigned *(.01 ≤ P < .05), **(.001 ≤ P < .01), ***(.0001 ≤ P). All the analyses and graphs were performed using GraphPad Prism 6 software (GraphPad, San Diego, CA).

2.15.1 | Schemes and cartoons

Schemes and cartoons were produced with Biorender.com.

3 | RESULTS

3.1 | Production and characterization of EV^{CSC} and EV^{DCC}

CSC were obtained by fluorescence-activated cell sorting (FACS) from the MDA-MB-231 ALDH1A1:tdTomato model, previously described and validated by our group[12] along with other breast cancer cell lines for example, MCF-7[33] and HCC1806.[38] Briefly, cells were stably transfected with a vector expressing the reporter tdTomato fluorescent protein under the control of the CSC ALDH1A1 promoter. This strategy allows the fluorescent tagging of ALDH1A1 expressing CSC, while nonfluorescent cells represent the DCCs subpopulation.[12]

Prior to EV production, in vitro cell propagation of CSC and DCC of MDA-MB-231 was optimized (Figure S1A-C). To maintain the stem features of CSCs (>95% tdTomato+) serum-free stem media was employed (Figure S1A) while DCCs were cultured in the presence of a minimal fraction (<2% tdTomato+) of CSCs (Figure S1B) to avoid dedifferentiation. Under these culture conditions, MDA-MB-231 CSCs showed significantly higher mRNA levels of prevalent stem gene reporters, *ALDH1A1*, *Nanog* and *Oct-4*, than MDA-MB-231 DCC (Figure 1A,B). Besides, phenotypic traits like cancer cell invasion also proved more accentuated for MDA-MB-231 CSC than for their MDA-MB-231 DCC counterpart (Figure 1C).

Thus, EVs were successfully isolated by charge neutralization-based precipitation from CSC and DCC cultures (Figure S1D-F). Both types of EVs presented pseudospherical morphologies as observed by cryoTEM and STORM imaging (Figures 1D and S2A,E) with a size distribution ranging from 100 to 300 nm in diameter. Nanoparticle tracking analysis (NTA) placed the main peak at 145 nm in diameter for both types of vesicles although a minor population of bigger particles could be detected in all samples (Figure 1F). Particle concentration of EVs samples was found in the same range, $1.035 \times 10^{10} \pm 0.235$ (particles/mL) for EVs^{CSC} and $2.665 \times 10^{10} \pm 0.835$ (particles/mL) for EVs^{DCC}. In addition, the presence of typical protein markers such as CD81, TSG101 and ALIX indicated that isolated EVs were enriched in exosomes (Figure 1G). Low β-tubulin occurrence in EVs samples confirmed them free from significant cell debris contamination. Furthermore, no differences in the cell uptake of EVs secreted by either CSC or DCC were observed when added to parental MDA-MB-231 cells or the lung fibroblast cell line CCD-19Lu. After incubation with fluorescently labeled EVs, a similar spotted fluorescent signal pattern was observed in both, tumor cells and fibroblasts, probably corresponding to clusters of EVs being gathered within endosomal vesicles (Figure S2B,E). Super resolution STORM imaging showed smaller particles matching the size of individual EVs (Figure S2C). Additional analysis performed by flow cytometry revealed no differences in the uptake kinetics profile between EVs^{CSC} and EVs^{DCC} by MDA-MB-231 cells (Figure S2D).

Interestingly, despite similarities in size, shape, internalization capacity and even EV-specific protein signature, discrepancies in the stemness related protein cargo were clearly detected. EVs^{CSC} presented higher levels of typical stemness protein markers such as ALDH1A1, CD44, SOX2 and E-cadherin than EVs^{DCC} (Figure 1H,I).

3.2 | EVs^{CSC} promote fibroblasts invasiveness and trigger angiogenesis

Once proved that EVs could load distinct biological cues depending on the differentiation state of their cell source, we explored the impact of these EVs on invasive capabilities of fibroblasts.

To this end, we first performed 3D invasion assays using spheroids formed by either CAFs of invasive ductal breast carcinoma (CAFs IDC) or lung fibroblasts (CCD-19Lu), previously treated with EVs^{CSC} and EVs^{DCC} for 48 hours. The 3D invasive capacity of fibroblasts was monitored by recording the number and length of strands branched from spheroids into the surrounding Matrigel/collagen matrix. As observed in Figure 2A-C CAFs IDC spheroids treated with EVs^{CSC} formed more (27 ± 1 vs 23 ± 1), and longer

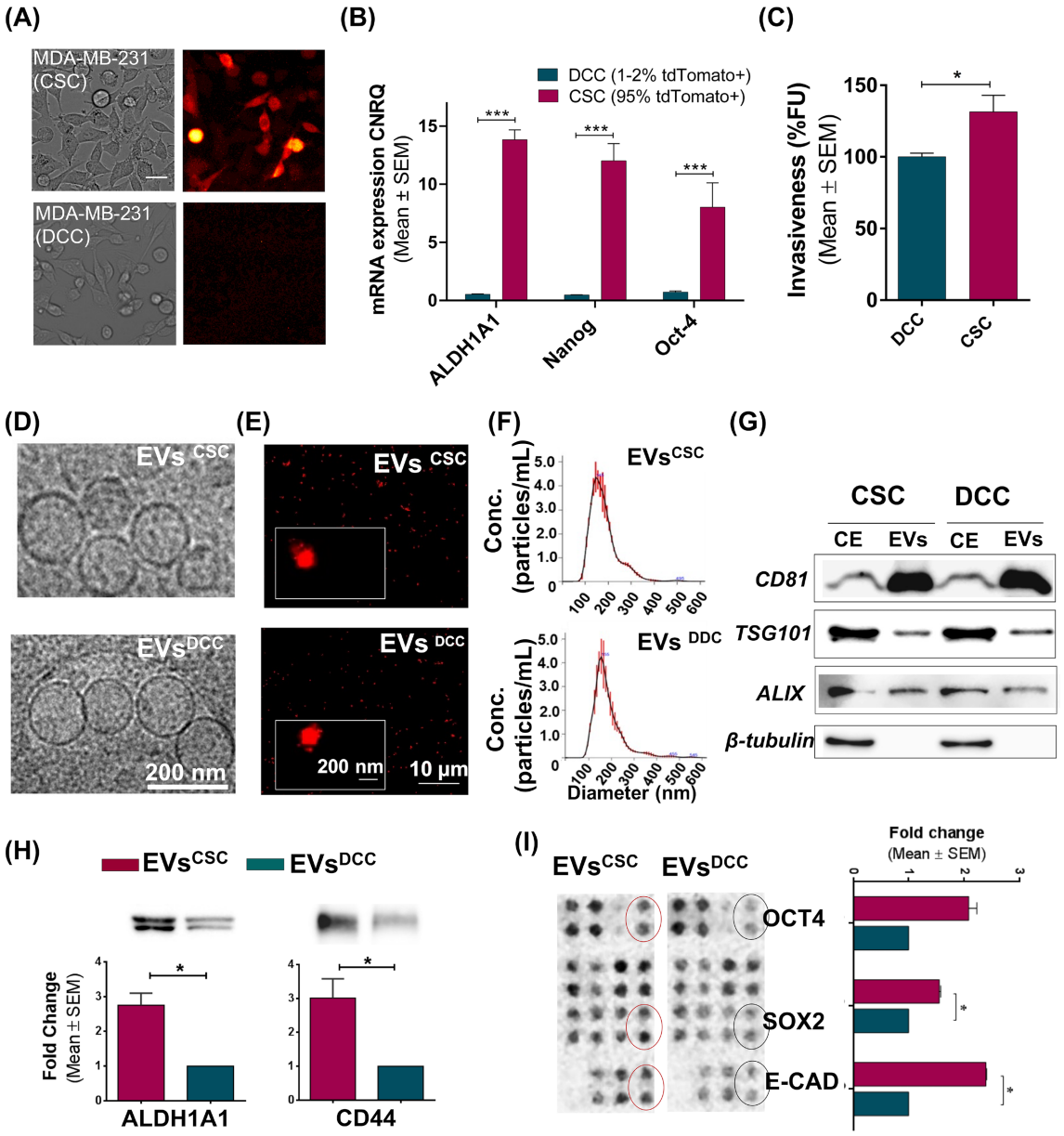

FIGURE 1 EVs^{CSC} and EVs^{DCC} isolation and characterization. (A) Representative images of CSCs and DCCs analyzed for tdTomato fluorescence, scale bar = 25 µm. (B) Gene expression of stemness reporters *ALDH1A1*, *Nanog* and *Oct-4* detected by qPCR for MDA-MB-231 subpopulations. CSC refers to tdTomato + cells cultured in stem cell maintenance media while DCC indicates cells cultured with a minimal presence of CSC (1%-2%) to avoid de-differentiation. CNRQ stands for Calibrated Normalized Relative Quantity with respect to GAPDH and Actin housekeeping genes. (C) 2D laminin invasion assay comparing CSC and DCC cells. (D) CryoTEM imaging of isolated EVs^{CSC} and EVs^{DCC}. (E) Stochastic Optical Resolution Microscopy (STORM) imaging of isolated EVs previously labeled with DiD. (F) Size distribution by nanoparticle tracking analysis (NTA) of EVs^{CSC} and EVs^{DCC}. (G) EVs typical markers, CD81, TSG101 and ALIX and cell lysate control, β-tubulin identified by Western blot. Twenty micrograms of total protein was loaded per lane and cell extracts (CE) were included as controls. (H) ALDH1A1 and CD44 protein cargo in EV^{CSC} and EVs^{DCC} examined by Western blot. (I) Protein cargo of EV^{CSC} and EVs^{DCC} assayed with a Human Pluripotent Stem Cell Array, showing higher content of OCT4, SOX2 and E-Cadherin in EV^{CSC}. In H and I, quantification of blots are shown as the fold change in the band/dot intensity of EVs^{CSC}/EVs^{DCC}. Differences are significant for ALDH1A1, CD44, SOX2 and E-Cadherin (*$P < .05$)

strands (260.7 ± 6.7 µm vs 238.4 ± 5.8 µm) than the ones supplemented with the EVs^{DCC} fraction. Lung fibroblast spheroids treated with EVs^{CSC} also displayed significantly higher number of strands (58 ± 3 vs 30 ± 2) and longer, (156.8 ± 3.4 µm vs 129.9 ± 3.9 µm) when compared to EVs^{DCC} treated ones (Figure 2D-F). Supporting these results, CCD-19Lu lung fibroblasts revealed higher α-SMA levels after treatment with EVs^{CSC} in comparison to EVs^{DCC} treated cells (Figure S3A,B). Interestingly, α-SMA staining and subsequent CAF infiltration was also markedly more intense in orthotopic primary tumors formed by MDA-MB-231 CSCs, assuming in such situation a predominant presence of EV^{CSC}, in comparison to the ones generated from MDA-MB-231 DCCs (Figure S3C-E).

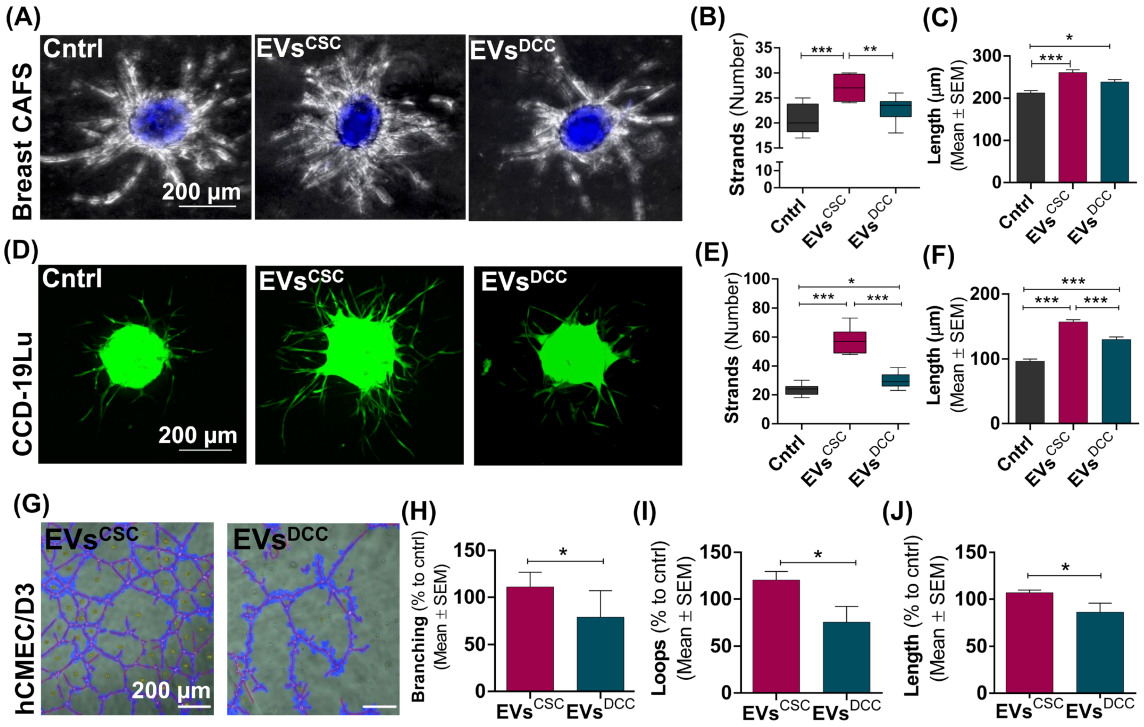

FIGURE 2 MDA-MB-231 EVs^{CSC} activate myCAFs populations and trigger angiogenesis. (A) Representative Z stack projection images of 3D invasive spheroids of breast CAFs educated with EVs^{CSC} or EVs^{DCC}. Graphs displaying the number (B) and length (C) of invasive strands from breast CAFs spheroids. Box plots corresponding to the representation of the number of strands show the median value as an horizontal line. Bar charts display the mean value as indicated in *y*-axis. (D) Representative Z stack projection images of 3D invasive spheroids lung CCD-19Lu fibroblasts educated with EVs^{CSC} or EVs^{DCC}. Graphs displaying the number (E) and length (F) of invasive strands from CCD-19Lu spheroids represented as described above. (G) Representative images of in vitro tube formation assay performed with endothelial cells (hCMEC/D3) treated with either EVs^{CSC} or EVs^{DCC}, the number of branching points (H), total loops (I) and tubes length (J) referred to those in nontreated control cells are represented in the graphs (*P < .05; **P < .01; ***P < .001)

Additionally, the influence of EVs^{CSC} and EVs^{DCC} on angiogenesis was assessed by challenging endothelial cells (hCMEC/D3) with both types of EVs and recording their in vitro tube formation capability. Results showed that EVs^{CSC} significantly enhanced the formation of new tubes in terms of length ($P = .0459$), and complexity of the network, as displayed by the relative increase in the number of branching points ($P = .0347$) and the number of total loops completed ($P = .0176$), in comparison to hCMEC/D3 treated with EVs^{DCC} (Figure 2G-J).

3.3 | EVs^{DCC} impact cancer cells plasticity via fibroblasts stimulation of cytokine secretion

To further investigate the EV mediated cancer cell—TME crosstalk, we incubated CCD-19Lu fibroblasts with either EVs^{CSC} or EVs^{DCC}, washed the cells to remove exogenous EVs and allowed them to secrete bioactive factors. CCD-19Lu conditioned media (CM) was collected for cytokine analysis and further employed to challenge MDA-MB-231 cells (scheme displayed in Figure 3A and S3H). Cytokine arrays showed that EVs^{DCC} triggered the fibroblasts secretion of cytokines IL-8, IL-6 and CXCL1. Specifically, IL-8 and IL-6 levels increased 61.5- and 2.7-fold, respectively, when compared to untreated controls. EVs^{DCC} also induced the release of CXCL1 in recipient CCD-19Lu cells, which was undetectable in the control CM. Conversely, incubation with EVs^{CSC} caused a decrease in IL-6 secretion compared to untreated cells (Figure 3B). These results were further confirmed by IL-6 and IL-8 gene expression analysis on CCD-19Lu cells. EVs^{DCC} promoted higher mRNA levels of *IL-6* and *IL-8*, 6.4- and 100-fold, respectively (Figure 3C).

Furthermore, we also analyzed the response of MDA-MB-231 cells to the CM of EV-pretreated CCD-19Lu cells. MDA-MB-231 cells cultured in EVs^{DCC}-CM showed a remarkable boost in the expression of *ALDH1A1*, *Nanog* and *Oct-4*, with 3.6 ± 0.7; 5.54 ± 0.4 and 4.6 ± 0.4 times higher expressions than the untreated control, respectively (Figure 3D). Contrarywise, EVs^{CSC}-CM did not display any relevant effect on the stemness gene expression profile of MDA-MB-231 cells (Figure 3D). To further validate the results obtained with EVs^{DCC}-CM, MDA-MB-231 cell cultures were incubated with recombinant IL-8 and IL-6, the two main cytokines upregulated by EVs^{DCC} in CCD-19Lu cells. Recombinant ILs had a similar effect to the EVs^{DCC}-CM in MDA-MB-231 cells (Figure 3E). Specifically, IL-6 significantly increased the expression of *ALDH1A1*, *Nanog* and *ABCGC1* while IL-8 exerted a substantial upregulating effect on *Nanog*. In agreement with the previous results, MDA-MB-231 ALDH:tdTomato cells cultured with EVs^{DCC}-CM displayed higher numbers of tdTomato+ cells, as a result of the activation of the ALDH1A1 promoter and the stemness phenotype

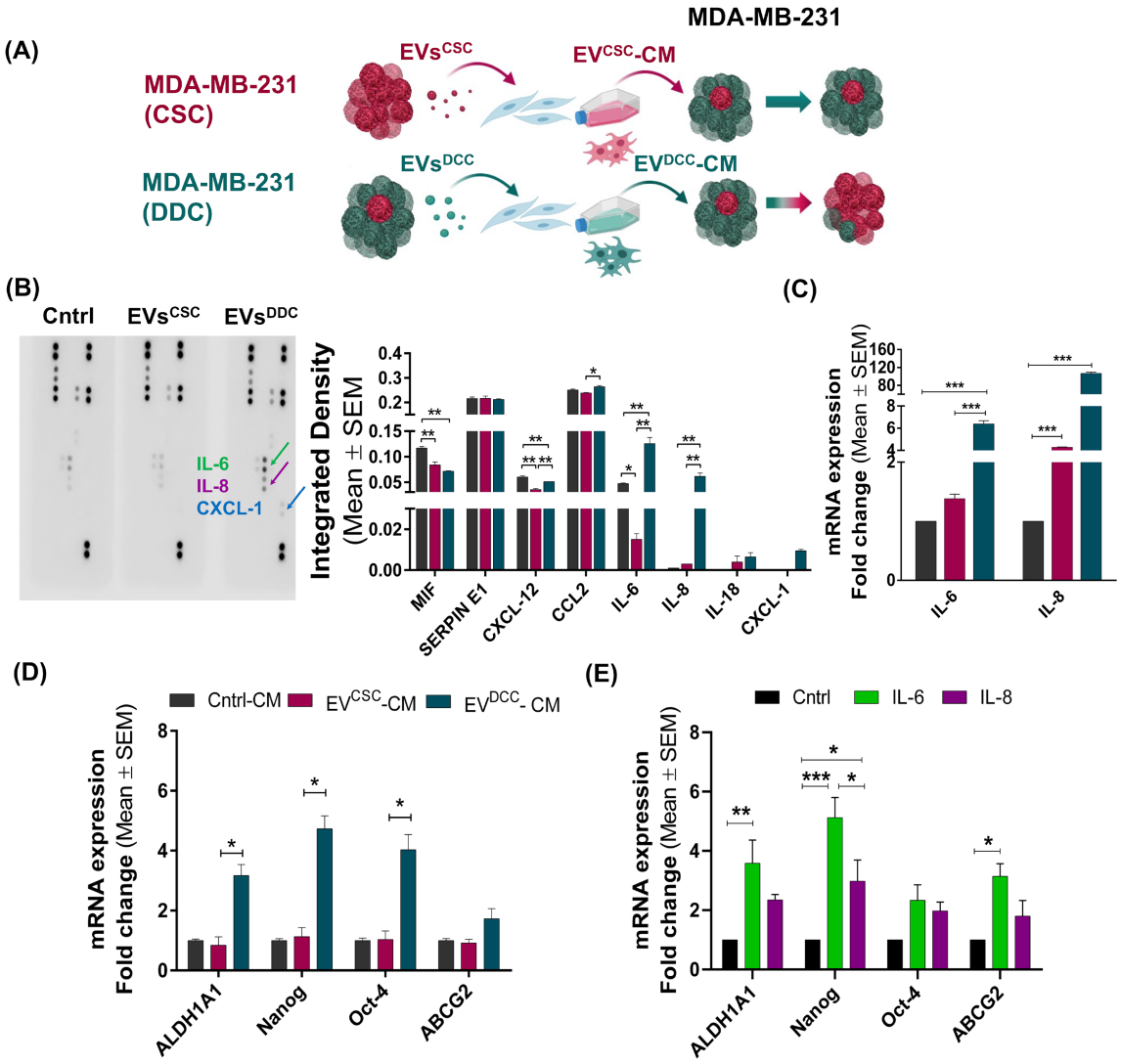

FIGURE 3 EVs^{DCC} promote iCAFs activation and regulate cancer cells plasticity. (A) Scheme of the experimental approach, CCD-19Lu fibroblasts were educated with either MDA-MB-231 EVs^{CSC} or EVs^{DCC} and CCD-19Lu conditioned media (CM) were collected for analysis and further supplemented to MDA-MB-231 parental cells. (B) Total human profiler cytokine array performed in CCD-19Lu CM and densitometric quantification of the obtained signal. (C) Gene expression of IL-6 and IL-8 in CCD-19Lu cells conditioned with MDA-MB-231 EVs^{CSC} or EVs^{DCC} by qPCR. (D) Effect of CCD-19Lu CM obtained after treatment with MDA-MB-231 EVs^{CSC} or EVs^{DCC} in parental MDA-MB-231 stemness gene expression by qPCR. (E) Gene expression in MDA-MB-231 cells treated with 20 ng/mL of recombinant IL-8 or IL-6 by qPCR (*P < .05; **P < .01; ***P < .001)

(Figure S3I). Additionally, the resistance of MDA-MB-231 cells to paclitaxel (PTX), a common chemotherapeutic drug, was increased in cells treated with EV^{DCC}-CM when compared to control cells and to MDA-MB-231 cells cultured in EVs^{CSC}-CM (Figure S3J), showing that this CSC related feature was also activated by EV^{DCC}-activated fibroblasts. These results suggested that EVs^{DCC} played an important role on the activation of pro-stem iCAFs subpopulations.

3.4 | EVs^{CSC} boosts lung metastasis

In order to explore whether EVs^{CSC} and EVs^{DCC} also played a different role in the activation of stromal cells in vivo, we studied the biodistribution and the lung annidation of EVs derived from MDA-MB-231 cancer cells.

First, the biodistribution profile of DiR labeled EVs was analyzed 24 hours after intravenous administration. Note that although lipophilic dyes such as DiR can present some technical issues regarding potential dye transference to off-target cells their use has been proven reliable for in vitro and short-term in vivo assays.[39] As shown in Figure 4A similar distribution patterns were observed for both EVs^{CSC} and EVs^{DCC}, with a major accumulation in lungs, followed by liver and spleen. This profile confirmed the capacity of our EVs to primarily reach the lungs, as relevant future metastatic site, validating the following EV mediated lung conditioning assays. Slight differences between EV^{CSC} and EVs^{DCC} biodistribution were further explored by

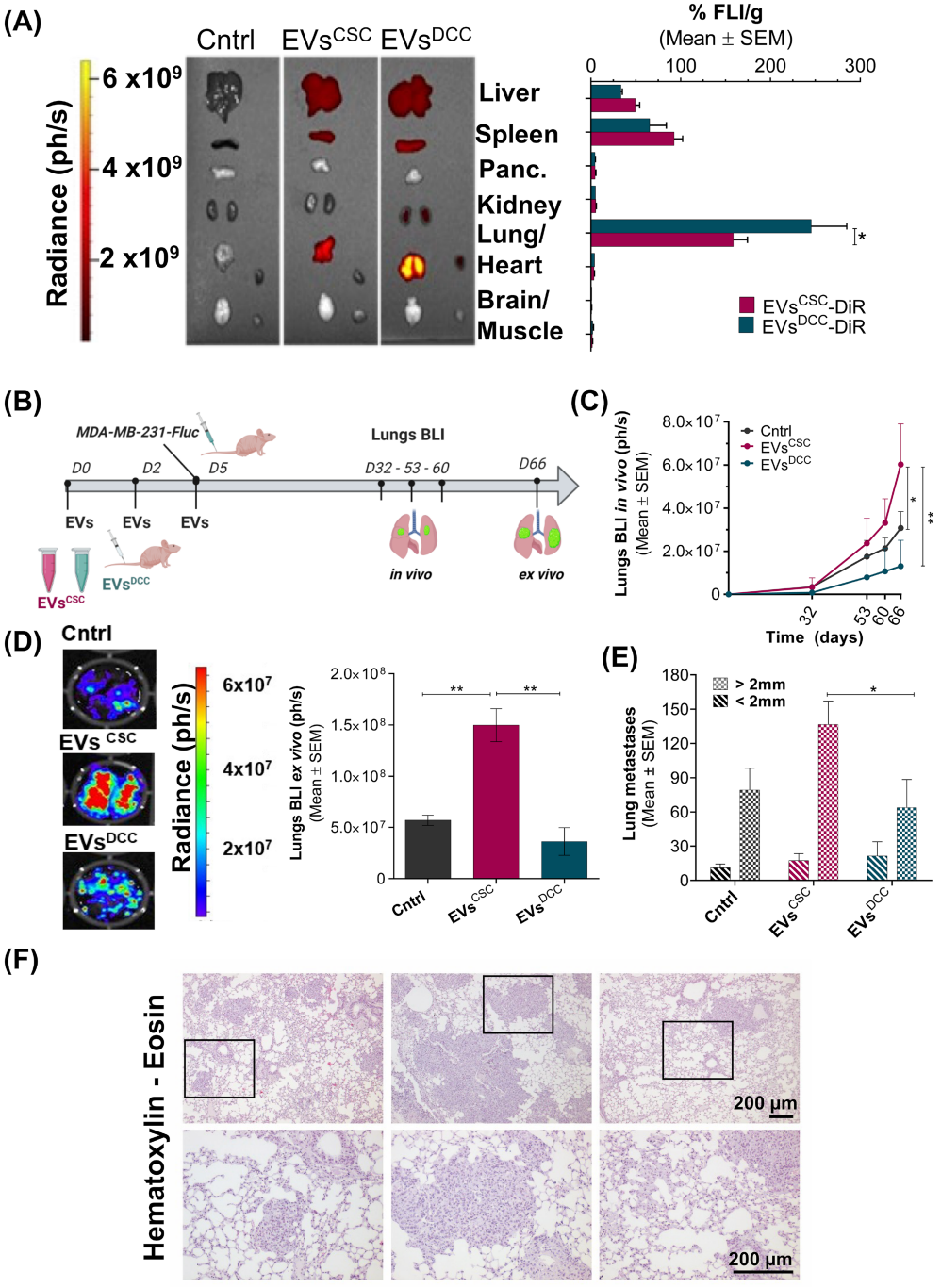

FIGURE 4 EVs^{CSC} conditioning boosts lung metastasis in vivo.
(A) Biodistribution of DiR-labeled EVs by fluorescence imaging (FLI) 24 hours postadministration. *Left panels*, representative FLI images of organs in mice administered with EV^{CSC} or EV^{DCC}. *On the right*, graph displaying ex vivo FLI values normalized with respect to the untreated controls and represented as % of the total FLI/g. (B) Schematic representation of the in vivo study analyzing the EVs^{CSC} and EVs^{DCC} conditioning effect on MDA-MB-231 lung metastasis. EVs and cells were administered by intravenous injection through the tail vein. (C) Lung metastasis growth monitored by in vivo luciferase-based BLI of mice pretreated with EVs^{CSC} and EVs^{DCC} and injected with MDA-MB-231 expressing luciferase cells along the time. (D) *On the left*, representative ex vivo BLI images of lungs at the end point for each condition. *On the right*, BLI ex vivo quantification of lungs at the endpoint. (E) Total number of macro and micrometastasis in the lungs manually counted for control, EVs^{CSC} and EVs^{DCC} preconditioned animals.
(F) Representative Hematoxylin/Eosin staining in lung sections from different treatment groups (*P < .05; **P < .01)

confocal imaging (Figure S4A) and main integrins (ITG) expression, related to lung tropism, assessed by western blot. Higher expression of ITGα6 was detected on EVs^{DCC} but no difference was evident for ITGβ1 (Figure S4B).

After confirming cancer cell derived EVs were able to reach the lungs we proceeded with the functional assessment of premetastatic niche conditioning. To this end, two groups of NOD/SCID mice received i.v. administrations of 75 µg of either EVs^{CSC} or EVs^{DCC} every other day during 5 days, corresponding to 3 to 6 × 10^8 particles/bolus. Mice from the control group were administered with equivalent volumes of PBS following the same regimen. Subsequently, luciferase expressing MDA-MB-231 cancer cells were i.v. injected into the tail vein and lung metastasis was evaluated over time (Figure 4B). In vivo bioluminescence imaging (BLI) showed that mice preconditioned with EVs^{CSC} displayed significantly more BLI signal in the lungs than control mice or those pretreated with EVs^{DCC} (Figure 4C). These results were confirmed by ex vivo BLI determination. Accordingly, lungs excised from animals treated with EVs^{CSC} reached 1.50 ± 0.16 × 10^8 ph/s, while lungs from EVs^{DCC} pretreated mice displayed only 0.36 ± 0.13 × 10^8 ph/s, in the same range than untreated animals, 0.57 ± 0.05 × 10^8 ph/s (Figure 4D).

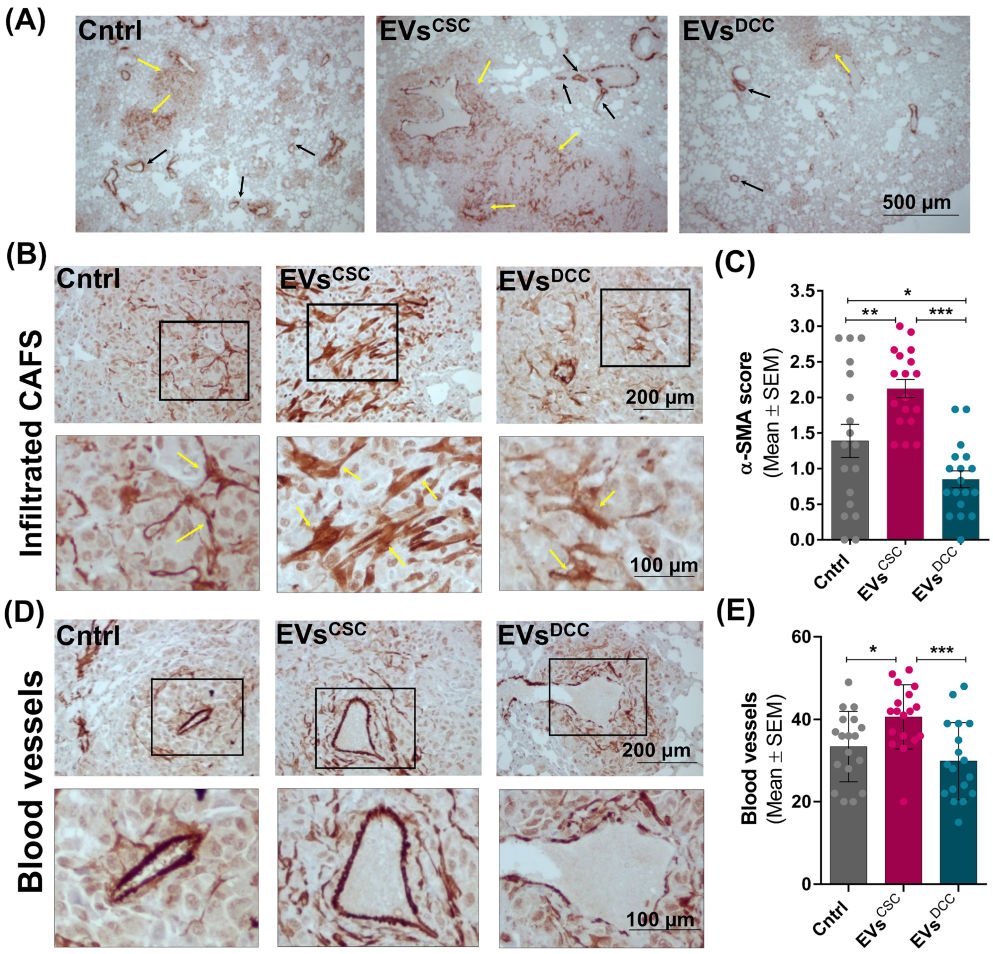

FIGURE 5 EVs^{CSC} increase the incidence of CAFs and triggers angiogenesis in lungs. (A) Low magnification images showing α-SMA staining on MDA-MB-231 lung metastases of mice educated with EVs^{CSC}, EVs^{DCC} and untreated controls. Yellow arrows indicate fibroblasts infiltrations; black arrows indicate blood vessels. (B) Detail of infiltrating cancer-associated fibroblasts (CAFs) in lungs tissue sections from the distinct mouse groups. Yellow arrows indicate cells with fibroblast-like morphology. (C) Semi-quantitative determination of α-SMA immunostaining in lung metastases. Lung sections were analyzed and labeling scores qualitatively attributed, values ranging from 0 (0% covered area); to 3 (100% covered area). (D) Detail of blood vessels in lungs tissue sections of indicated mice groups. Insets show blood vessels at higher magnification. (E) Total number of blood vessels in random fields from lung metastases sections (*P < .05; **P < .01; ***P < .001)

Furthermore, the number of lung metastasis was individually counted revealing a remarkable impact of EVs^{CSC} conditioning on the macrometastatic burden (metastatic foci >2 mm). Precisely, the number of lung macrometastasis per mouse achieved 137 ± 21 for EVs^{CSC} treated group while EVs^{DCC} treated group and untreated animals produced significantly lower numbers 64 ± 24 and 79 ± 19, respectively. No relevant differences in the micrometastasis count were detected (Figure 4E). Additionally, results on lung BLI intensity and macroscopic metastasis counting were confirmed by histopathological evaluation on hematoxylin-eosin sections (Figure 4F) and by immunohistochemistry against vimentin (Figure S5A,B). Notably, the lungs of the animals injected with EVs^{CSC} presented very extended metastatic lesions in the lungs.

3.5 | EVs^{CSC} promote PMN remodeling via myCAFs activation and angiogenesis enhancement

Given the dramatic promotion of the metastatic burden by EVs^{CSC} we further studied their effect on lung stromal cells, namely lung fibroblasts and endothelial cells. To evaluate the presence of activated fibroblasts derived from EVs education in metastatic lesions, α-SMA immunostaining was performed in lung tissues from animals previously conditioned with either EVs^{CSC} or EVs^{DCC} and subsequently injected with MDA-MB-231 cells (Figure 5A). Detail of α-SMA immunostaining of fibroblast like cells can be observed in Figure 5B. Higher numbers of α-SMA+ CAFs in the lungs of animals treated with EVs^{CSC} were observed within the metastatic lesions (mean score for α-SMA staining = 2.125). Control animals and mice conditioned with EVs^{DCC} also showed a clear signal for the α-SMA marker, but with significantly lower scores (0.85; and 1.38, respectively; Figure 5C). Moreover, biodistribution studies showed that α-SMA immunostaining was also more intense in healthy lungs of animals administered with EVs^{CSC} in comparison to EVs^{DCC}-treated mice, supporting a direct role of EVs conditioning the lungs rather than an effect on MDA-MB-231 cells (Figure S3F,G).

Of note, α-SMA also tagged vascular endothelial cells and enabled thus to assess EVs impact on angiogenesis. Blood vessels (b.v) structures, detailed in Figure 5D, were counted in random lung sections. Concomitantly with previous in vitro results, EVs^{CSC} displayed higher angiogenic potential in vivo than the EVs^{DCC} fraction. Lungs from animals injected with EVs^{CSC} exhibited the highest b.v. number (40.61 ± 1.833 b.v./field), compared to EVs^{DCC} injected animals (29.83 ± 2.22 b.v./field) and control animals (33.38 ± 2.02 b.v./field; Figure 5E). Additionally, CD31 immunostaining on the same lung sections displayed matching staining of b.v structures

confirming α-SMA results (Figure S5C). On the other hand, EVs^{DCC} displayed no significant in vivo effect in terms of functional TME activation favoring metastatic cells growth.

4 | DISCUSSION

Intercellular communication mediated by EVs has been proved crucial in the regulation of multiple pathological processes during tumor growth, maintenance and spread.[19] However, in the TNBC context, whose tumors are composed by heterogeneous, highly plastic polyclonal cell populations, EV-mediated communication studies have been frequently biased due to insufficient information regarding the specific phenotype and cell state of the EV secreting cancer cells.

In the present work, we have established an experimental setup consisting of the use of two different breast cancer cell subpopulations isolated from the MDA-MB-231 TNBC cell line that are distant in the stemness axis. This approach allowed us to isolate and characterize two distinct EVs subpopulations, EVs^{DCC} secreted by MDA-MB-231 cells with a minimal presence of CSCs and EVs^{CSC} produced by MDA-MB-231 highly enriched in CSCs. Our results showed both types of EVs as essentially identical entities regarding their morphometric properties, namely particle size and shape. Besides, no significant differences were observed in terms of cell internalization capacity in either tumor cells or stromal cells, specifically in CCD-19Lu lung fibroblast. In addition, upon intravenous administration in mouse, the biodistribution profile was in accordance with previous reports on EVs derived from TNBC cells. EVs showed a marked tendency to accumulate into their primary metastatic sites, likely directed by the integrin expression onto the EVs surface.[27,40] Important similarities were also displayed concerning the specific EVs protein marker expression, for example, CD81, TSG101 or ALIX but remarkably, EVs contents between EVs^{CSC} and EVs^{DCC} varied in their protein cargo (eg, CD44, ALDH1A1 or SOX2 being more abundant in EVs^{DCC}). Such differences suggested the possibility for EVs^{CSC} and EVs^{DCC} of delivering distinctive signaling cues and therefore performing distinct roles in TNBC intercellular communication.

In this regard, multiple studies have shown that tumor-derived EVs can activate normal fibroblasts, as main elements of tumor stroma, to acquire malignant CAF phenotypes with significant incidence in disease progression.[22,27] Here, we identified two distinct EVs-dependent communication avenues between cancer cells and CAFs that were controlled by the particular stem cell state of the EVs secreting cancer cells.

On the one hand, EVs^{DCC} activated the secretion of pro-stemness cytokines IL-6 and IL-8 on CAFs, likely promoting their activation towards iCAFs, even though the influence of other signaling molecules cannot be excluded. Remarkably, these iCAFs were able to, in turn, induce tumor cell de-differentiation. The capacity of CAFs to regulate tumor plasticity through secretion of cytokines has already been extensively examined.[41,42] Particularly, IL-6 and IL-8 cytokines have been described to operate via activation of STAT3 and NF-κB signaling pathways, inducing the expression of stem genes and the subsequent transition of tumor cells towards CSC-like states.[43-45] In agreement with our data, Su et al. recently described a subpopulation of fibroblasts responsible for providing a constant source of paracrine IL-6 and IL-8 that maintained a feedback loop sustaining CSC stemness via NF-kB pathway activation in breast cancer.[13] However, in our in vivo models, EVs^{DCC} produced a negligible impact on the metastatic burden after animal preconditioning. In this sense, the use of NOD/SCID immunodeficient mice could be oversimplifying critical interactions with other relevant stroma fractions, like immune cells, that have also been closely related to CSC occurrence.[18,46,47]

On the other hand, EV^{CSC} triggered the activation of a myofibroblastic subset of CAFs, myCAFs, with a remarkable potential for ECM remodeling and significant expression of the myofibroblast marker α-SMA. myCAFs have been described as cells capable of generating ECM tracks to guide cancer cells at primary tumor and metastatic sites, largely influencing tumor local invasion.[29,36,48] Our experiments revealed that EVs^{CSC} preconditioning increased the extent of the macrometastasis burden in mice lungs, indicating that EVs^{CSC} strongly promoted the dissemination of malignant cells into the lungs by creating a tumor cell growth supportive niche. Consequently, EVs^{CSC} treated animals showed higher presence of α-SMA+ CAFs and more blood vessels in lungs. This EV^{CSC} activity was supported by previous in vitro results showing EVs^{CSC} as potent activators of the invasiveness of breast and lung fibroblasts as well as angiogenic enhancers. In addition, stronger signals of α-SMA were detected in lungs from healthy animals after EVs^{CSC} administration, reinforcing EVs^{CSC}-mediated activation of resident lung fibroblasts. In the same line, a notable α-SMA staining and CAF infiltration were also observed in primary tumors exclusively generated from MDA-MB-231 CSC-like cells, where higher amounts of the EVs^{CSC} subset are expected to be secreted to the TME. To the best of our knowledge, no specific studies describing CSC-derived EVs contribution in premetastatic conditioning have been previously published. However, in agreement with our observations, EVs isolated from particularly malignant cells, for example, drug-resistant tumor cells, often associated with CSCs-like phenotypes, have been shown to provide higher metastatic potential than the ones from the parental cell lines.[49] Altogether these results suggest that EVs secreted by CSC-like cells are crucial signaling platforms for triggering niche remodeling at the metastatic sites.

Our results concur with recent studies highlighting CAFs heterogeneity among different tumor types.[13,30,31] Single-cell analysis of TNBC stroma clustered CAFs into these two main, myCAFs and iCAFs, groups albeit significant intragroup heterogeneity.[28] In other cancer types, for example, pancreatic cancer, CAF subpopulations with different levels of α-SMA have been identified within the tumor. One being myofibroblastic, myCAFs profile, $\alpha\text{-SMA}^{high}\text{IL-6}^{low}$ and the other one pro-inflammatory iCAFs, $\alpha\text{-SMA}^{low}\text{IL-6}^{high}$.[50] Nevertheless, up to date, the mechanisms driving specific activation of certain CAF phenotypes have been not clarified. Here, we present evidence that CAF heterogeneous activation may be governed by distinct subpopulations of tumor-secreted EVs, defined by the particular differentiation state of the cell origin.

5 | CONCLUSION

We have identified two distinct subsets of EVs, namely EVs^{CSC} and EVs^{DCC}, according to the stem cell state from their cell source. These EV

subsets displayed markedly different activities in heterotypic cell communication in TNBC models. EVs^{DCC} could indirectly influence tumor cell dedifferentiation state by the stimulation of a cytokine secretory CAFs phenotype while EVs^{CSC} triggered the activation of a distinct and specific myofibroblastic CAF subpopulation, facilitating local invasion and growth. Accordingly, EVs^{CSC} also displayed proangiogenic potential and postulated as principal activators of niche modulation enabling metastatic growth.

AUTHOR CONTRIBUTIONS

Conceptualization: Patricia González-Callejo, Petra Gener, Simó Schwartz Jr. and Joaquin Seras-Franzoso; methodology: Patricia González-Callejo, Zamira V. Díaz-Riascos, Sefora Conti, Patricia Cámara-Sánchez, Roger Riera, Sandra Mancilla, Miguel García-Gabilondo, Vicente Peg, Anna Labernadie, Lorenzo Albertazzi and Joaquin Seras-Franzoso; resources: Diego Arango, Anna Rosell, Xavier Trepat, Lorenzo Albertazzi and Ibane Abasolo; supervision: Joaquin Seras-Franzoso, Anna Labernadie, Anna Rosell, Lorenzo Albertazzi and Ibane Abasolo; project administration: Petra Gener and Simó Schwartz Jr; writing: *First draft*: Patricia González-Callejo and Joaquin Seras-Franzoso, *Final draft*: all authors. The work reported in the paper has been performed by the authors, unless clearly specified in the text.

ACKNOWLEDGEMENTS

We are indebted to Unitat of Alta Tecnologia (UAT) at the Vall d'Hebron Research Institute for their assistance in flow cytometry and confocal microscopy procedures. We also thank to "Servei de Microscòpia" at the Universitat Autònoma de Barcelona (UAB) where electron microscopy analysis took place. Additionally, part of physicochemical EVs characterization and all the in vivo studies were performed by the Unique Scientific and Technical Infrastructures (ICTS) "NANBIOSIS," at the Bioengineering, Biomaterials and Nanomedicine Research Center (CIBER-BBN), specifically NTA analysis was carried out at Unit 6:Biomaterial Processing and Nanostructuring and animal experimentation at Unit 20: in vivo experimental platform (www.nanbiosis.es). We also thank Dr Pedro Fuentes and Marion Martinez for kindly providing ITGβ1 and ITGα6 antibodies, respectively.

FUNDING INFORMATION

Our study was supported by ISCIII PI20/01474 (co-founded by Fondo Europeo de Desarrollo Regional [FEDER]) granted to Simó Schwartz Jr and Petra Gener, the 2017-SGR-638 and -1427 form the Generalitat de Catalunya to Simó Schwartz Jr and Anna Rose, respectively, and PENTRI-2 from CIBER-BBN granted to Ibane Abasolo. Anna Labernadie is recipient of Obra Social "La Caixa" Junior Leader Postdoctoral Fellowship, (LCF/BQ/PR18/11640001). Joaquin Seras-Franzoso was awarded with an Asociación Española Contra el Cancer (AECC), (AIO14142112SERA) post-doctoral fellowship.

CONFLICT OF INTEREST

Vicente Peg has received fees as consultant, participated in advisory boards or received travel grants from Roche, Sysmex, MSD, AstraZeneca, Bayer, Daiichi-Sankyo and Exact Sciences. The rest of the authors declare no potential conflict of interest.

DATA AVAILABILITY STATEMENT

The data that support the findings of our study are available from the corresponding author upon reasonable request.

ETHICS STATEMENT

Animal care was handled in accordance with the Guide for the Care and Use of Laboratory Animals of the Vall Hebron University Hospital Animal Facility, and the experimental procedures were approved by the Animal Experimentation Ethical Committee at the institution (approval number CEA-OH/9467/2).

ORCID

Diego Arango https://orcid.org/0000-0003-2953-3284
Joaquin Seras-Franzoso https://orcid.org/0000-0002-7893-4773

REFERENCES

1. Fragomeni SM, Sciallis A, Jeruss JS. Molecular subtypes and local-regional control of breast cancer. *Surg Oncol Clin N Am*. 2018;27:95-120.
2. Bray F, Ferlay J, Soerjomataram I, Siegel RL, Torre LA, Jemal A. Global cancer statistics 2018: GLOBOCAN estimates of incidence and mortality worldwide for 36 cancers in 185 countries. *CA Cancer J Clin*. 2018;68:394-424.
3. Wahl GM, Spike BT. Cell state plasticity, stem cells, EMT, and the generation of intra-tumoral heterogeneity. *NPJ Breast Cancer*. 2017;3:14.
4. Coates JT, Sun S, Leshchiner I, et al. Parallel genomic alterations of antigen and payload targets mediate polyclonal acquired clinical resistance to Sacituzumab Govitecan in triple-negative breast cancer. *Cancer Discov*. 2021;11:2436-2445.
5. Ma F, Li H, Wang H, et al. Enriched CD44(+)/CD24(−) population drives the aggressive phenotypes presented in triple-negative breast cancer (TNBC). *Cancer Lett*. 2014;353:153-159.
6. Ginestier C, Hur MH, Charafe-Jauffret E, et al. ALDH1 is a marker of normal and malignant human mammary stem cells and a predictor of poor clinical outcome. *Cell Stem Cell*. 2007;1:555-567.
7. Acharyya S, Oskarsson T, Vanharanta S, et al. A CXCL1 paracrine network links cancer chemoresistance and metastasis. *Cell*. 2012;150:165-178.
8. Albrengues J, Shields MA, Ng D, et al. Neutrophil extracellular traps produced during inflammation awaken dormant cancer cells in mice. *Science*. 2018;361:eaao4227. doi:10.1126/science.aao4227
9. Najafi M, Mortezaee K, Majidpoor J. Cancer stem cell (CSC) resistance drivers. *Life Sci*. 2019;234:116781.
10. Zomer A, Ellenbroek SIJ, Ritsma L, Beerling E, Vrisekoop N, Van Rheenen J. Intravital imaging of cancer stem cell plasticity in mammary tumors. *Stem Cells*. 2013;31:602-606. doi:10.1002/stem.1296
11. Fumagalli A, Oost KC, Kester L, et al. Plasticity of Lgr5-negative cancer cells drives metastasis in colorectal cancer. *Cell Stem Cell*. 2020;26:569-578.e7.
12. Gener P, Rafael D, Seras-Franzoso J, et al. Pivotal role of AKT2 during dynamic phenotypic change of breast cancer stem cells. *Cancers*. 2019;11:1058.
13. Su S, Chen J, Yao H, et al. CD10+GPR77+ cancer-associated fibroblasts promote cancer formation and chemoresistance by sustaining cancer stemness. *Cell*. 2018;172:841-856.e16.
14. Tsuyada A, Chow A, Wu J, et al. CCL2 mediates cross-talk between cancer cells and stromal fibroblasts that regulates breast cancer stem cells. *Cancer Res*. 2012;72:2768-2779.
15. Bartosh TJ, Ullah M, Zeitouni S, Beaver J, Prockop DJ. Cancer cells enter dormancy after cannibalizing mesenchymal stem/stromal cells (MSCs). *Proc Natl Acad Sci USA*. 2016;113:E6447-E6456.

16. Ji Z, He L, Regev A, Struhl K. Inflammatory regulatory network mediated by the joint action of NF-kB, STAT3, and AP-1 factors is involved in many human cancers. *Proc Natl Acad Sci USA*. 2019;116:9453-9462.
17. Bliss SA, Sinha G, Sandiford OA, et al. Mesenchymal stem cell-derived exosomes stimulate cycling quiescence and early breast cancer dormancy in bone marrow. *Cancer Res*. 2016;76:5832-5844.
18. Binenbaum Y, Fridman E, Yaari Z, et al. Transfer of miRNA in macrophage-derived exosomes induces drug resistance in pancreatic adenocarcinoma. *Cancer Res*. 2018;78:5287-5299.
19. Becker A, Thakur BK, Weiss JM, Kim HS, Peinado H, Lyden D. Extracellular vesicles in cancer: cell-to-cell mediators of metastasis. *Cancer Cell*. 2016;30:836-848.
20. Russell AE, Sneider A, Witwer KW, et al. Biological membranes in EV biogenesis, stability, uptake, and cargo transfer: an ISEV position paper arising from the ISEV membranes and EVs workshop. *J Extracell Vesicles*. 2019;8:1684862. doi:10.1080/20013078.2019.1684862
21. Chowdhury R, Webber JP, Gurney M, Mason MD, Tabi Z, Clayton A. Cancer exosomes trigger mesenchymal stem cell differentiation into pro-angiogenic and pro-invasive myofibroblasts. *Oncotarget*. 2015;6:715-731.
22. Fang T, Lv H, Lv G, et al. Tumor-derived exosomal miR-1247-3p induces cancer-associated fibroblast activation to foster lung metastasis of liver cancer. *Nat Commun*. 2018;9:191.
23. Tang MKS, Yue PYK, Ip PP, et al. Soluble E-cadherin promotes tumor angiogenesis and localizes to exosome surface. *Nat Commun*. 2018;9:2270.
24. Chen G, Huang AC, Zhang W, et al. Exosomal PD-L1 contributes to immunosuppression and is associated with anti-PD-1 response. *Nature*. 2018;560:382-386.
25. Li C, Qiu S, Jin K, et al. Tumor-derived microparticles promote the progression of triple-negative breast cancer via PD-L1-associated immune suppression. *Cancer Lett*. 2021;523:43-56.
26. Wendler F, Stamp GW, Giamas G. Tumor-stromal cell communication: small vesicles signal big changes. *Trends Cancer*. 2016;2:326-329.
27. Ji Q, Zhou L, Sui H, et al. Primary tumors release ITGBL1-rich extracellular vesicles to promote distal metastatic tumor growth through fibroblast-niche formation. *Nat Commun*. 2020;11:1211.
28. Wu SZ, Roden DL, Wang C, et al. Stromal cell diversity associated with immune evasion in human triple-negative breast cancer. *EMBO J*. 2020;39:e104063. doi:10.15252/embj.2019104063
29. Gaggioli C, Hooper S, Hidalgo-Carcedo C, et al. Fibroblast-led collective invasion of carcinoma cells with differing roles for RhoGTPases in leading and following cells. *Nat Cell Biol*. 2007;9:1392-1400.
30. Costa A, Kieffer Y, Scholer-Dahirel A, et al. Fibroblast heterogeneity and immunosuppressive environment in human breast cancer. *Cancer Cell*. 2018;33:463-479.e10.
31. Pelon F, Bourachot B, Kieffer Y, et al. Cancer-associated fibroblast heterogeneity in axillary lymph nodes drives metastases in breast cancer through complementary mechanisms. *Nat Commun*. 2020;11:404.
32. Wen SW, Lima LG, Lobb RJ, et al. Breast cancer-derived exosomes reflect the cell-of-origin phenotype. *Proteomics*. 2019;19:e1800180.
33. Gener P, Gouveia LP, Sabat GR, et al. Fluorescent CSC models evidence that targeted nanomedicines improve treatment sensitivity of breast and colon cancer stem cells. *Nanomedicine*. 2015;11:1883-1892.
34. Seras-Franzoso J, Díaz-Riascos ZV, Corchero JL, et al. Extracellular vesicles from recombinant cell factories improve the activity and efficacy of enzymes defective in lysosomal storage disorders. *J Extracell Vesicles*. 2021;10:e12058. doi:10.1002/jev2.12058
35. Conti S, Kato T, Park D, Sahai E, Trepat X, Labernadie A. CAFs and cancer cells co-migration in 3D spheroid invasion assay. *Methods Mol Biol*. 2021;2179:243-256.
36. Labernadie A, Kato T, Brugués A, et al. A mechanically active heterotypic E-cadherin/N-cadherin adhesion enables fibroblasts to drive cancer cell invasion. *Nat Cell Biol*. 2017;19:224-237.
37. Morancho A, Hernández-Guillamon M, Boada C, et al. Cerebral ischaemia and matrix metalloproteinase-9 modulate the angiogenic function of early and late outgrowth endothelial progenitor cells. *J Cell Mol Med*. 2013;17:1543-1553.
38. Cámara-Sánchez P, Díaz-Riascos ZV, García-Aranda N, et al. Selectively targeting breast cancer stem cells by 8-Quinolinol and Niclosamide. *Int J Mol Sci*. 2022;23:11760.
39. Lázaro-Ibánez E, Al-Jamal KT, Dekker N, et al. Selection of fluorescent, bioluminescent, and radioactive tracers to accurately reflect extracellular vesicle biodistribution in vivo. *ACS Nano*. 2021;15:3212-3227.
40. Hoshino A, Costa-Silva B, Shen T-L, et al. Tumour exosome integrins determine organotropic metastasis. *Nature*. 2015;527:329-335.
41. Kolář M, Szabo P, Dvořánková B, et al. Upregulation of IL-6, IL-8 and CXCL-1 production in dermal fibroblasts by normal/malignant epithelial cells in vitro: Immunohistochemical and transcriptomic analyses. *Biol Cell*. 2012;104:738-751. doi:10.1111/boc.201200018
42. van der Zee M, Sacchetti A, Cansoy M, et al. IL6/JAK1/STAT3 signaling blockade in endometrial cancer affects the ALDHhi/CD126+ stem-like component and reduces tumor burden. *Cancer Res*. 2015;75:3608-3622.
43. Singh JK, Farnie G, Bundred NJ, et al. Targeting CXCR1/2 significantly reduces breast cancer stem cell activity and increases the efficacy of inhibiting HER2 via HER2-dependent and -independent mechanisms. *Clin Cancer Res*. 2013;19:643-656.
44. Korkaya H, Liu S, Wicha MS. Regulation of cancer stem cells by cytokine networks: attacking Cancer's inflammatory roots: figure 1. *Clin Cancer Res*. 2011;17:6125-6129. doi:10.1158/1078-0432.CCR-10-2743
45. Iliopoulos D, Hirsch HA, Wang G, Struhl K. Inducible formation of breast cancer stem cells and their dynamic equilibrium with non-stem cancer cells via IL6 secretion. *Proc Natl Acad Sci USA*. 2011;108:1397-1402. doi:10.1073/pnas.1018898108
46. Lu H, Clauser KR, Tam WL, et al. A breast cancer stem cell niche supported by juxtacrine signalling from monocytes and macrophages. *Nat Cell Biol*. 2014;16:1105-1117.
47. Fan Q-M, Jing Y-Y, Yu G-F, et al. Tumor-associated macrophages promote cancer stem cell-like properties via transforming growth factor-beta1-induced epithelial–mesenchymal transition in hepatocellular carcinoma. *Cancer Lett*. 2014;352:160-168.
48. Glentis A, Oertle P, Mariani P, et al. Cancer-associated fibroblasts induce metalloprotease-independent cancer cell invasion of the basement membrane. *Nat Commun*. 2017;8:924.
49. Wang L, Yang G, Zhao D, et al. CD103-positive CSC exosome promotes EMT of clear cell renal cell carcinoma: role of remote MiR-19b-3p. *Mol Cancer*. 2019;18:86.
50. Öhlund D, Handly-Santana A, Biffi G, et al. Distinct populations of inflammatory fibroblasts and myofibroblasts in pancreatic cancer. *J Exp Med*. 2017;214:579-596.

SUPPORTING INFORMATION

Additional supporting information can be found online in the Supporting Information section at the end of this article.

How to cite this article: González-Callejo P, Gener P, Díaz-Riascos ZV, et al. Extracellular vesicles secreted by triple-negative breast cancer stem cells trigger premetastatic niche remodeling and metastatic growth in the lungs. *Int J Cancer*. 2023;152(10):2153-2165. doi:10.1002/ijc.34447